



**HAL**  
open science

## Sustained W-melting experiments on actively cooled ITER-like Plasma Facing Unit in WEST

Y Corre, A Grosjean, J Gunn, K Krieger, S Ratynskaia, O Skalli-Fettachi, C  
Bourdelle, S Brezinsek, V Bruno, N Chanet, et al.

► **To cite this version:**

Y Corre, A Grosjean, J Gunn, K Krieger, S Ratynskaia, et al.. Sustained W-melting experiments on actively cooled ITER-like Plasma Facing Unit in WEST. Physica Scripta, 2021. hal-03652668

**HAL Id: hal-03652668**

**<https://amu.hal.science/hal-03652668>**

Submitted on 26 Apr 2022

**HAL** is a multi-disciplinary open access archive for the deposit and dissemination of scientific research documents, whether they are published or not. The documents may come from teaching and research institutions in France or abroad, or from public or private research centers.

L'archive ouverte pluridisciplinaire **HAL**, est destinée au dépôt et à la diffusion de documents scientifiques de niveau recherche, publiés ou non, émanant des établissements d'enseignement et de recherche français ou étrangers, des laboratoires publics ou privés.

## Sustained W-melting experiments on actively cooled ITER-like Plasma Facing Unit in WEST

Y. Corre<sup>a,\*</sup>, A. Grosjean<sup>a</sup>, J. P. Gunn<sup>a</sup>, K. Krieger<sup>b</sup>, S. Ratynskaia<sup>c</sup>, O. Skalli-Fettachi<sup>a</sup>, C. Bourdelle<sup>a</sup>, S. Brezinsek<sup>d</sup>, V. Bruno<sup>a</sup>, N. Chanet<sup>a</sup>, J. Coenen<sup>d,e</sup>, X. Courtois<sup>a</sup>, R. Dejarnac<sup>f</sup>, E. Delmas<sup>a</sup>, L. Delpech<sup>a</sup>, C. Desgranges<sup>a</sup>, M. Diez<sup>a</sup>, L. Dubus<sup>a</sup>, A. Durif<sup>g</sup>, A. Ekedahl<sup>a</sup>, N. Fedorczak<sup>a</sup>, M. Firdaouss<sup>a</sup>, J-L. Gardarein<sup>h</sup>, J. Gaspar<sup>h</sup>, J. Gerardin<sup>f</sup>, C. Guillemaut<sup>a</sup>, M. Houry<sup>a</sup>, T. Loarer<sup>a</sup>, P. Maget<sup>a</sup>, P. Mandelbaum<sup>i</sup>, R. Mitteau<sup>a</sup>, M. Missirlian<sup>a</sup>, P. Moreau<sup>a</sup>, R. Nouailletas<sup>a</sup>, E. Nardon<sup>a</sup>, C. Pocheau<sup>a</sup>, A. Podolnik<sup>e</sup>, P. Reilhac<sup>a</sup>, X. Regal-Mezin<sup>a</sup>, C. Reux<sup>a</sup>, M. Richou<sup>a</sup>, F. Rigollet<sup>h</sup>, J-L. Schwob<sup>j</sup>, E. Thorén<sup>c</sup>, P. Tolas<sup>c</sup>, E. Tsitrone<sup>a</sup> and the WEST team\*

<sup>a</sup>CEA, Institute for Research on Fusion by Magnetic confinement, 13108 St-Paul-Lez-Durance, France

<sup>b</sup>Max-Planck-Institut für Plasmaphysik, 85748 Garching b. München, Germany,

<sup>c</sup>Space and Plasma Physics - KTH Royal Institute of Technology, SE-10044, Stockholm, Sweden,

<sup>d</sup>Forschungszentrum Jülich GmbH, Institut für Energie und Klimaforschung 52425 Jülich, Germany,

<sup>e</sup>Department of Engineering Physics, University of Wisconsin Madison, WI 53706 Madison, USA,

<sup>f</sup>Institute of Plasma Physics, Czech Academy of Sciences, 182 00 Prague, Czech Republic,

<sup>g</sup>Aix Marseille Univ, CNRS, Centrale Marseille, Institut Fresnel, Marseille, France,

<sup>h</sup>Aix Marseille Univ, CNRS, IUSTI, Marseille, France,

<sup>i</sup>Azrieli College of Engineering, 91035 Jerusalem, Israel

<sup>j</sup>Racah Institute of Physics, The Hebrew University, 91904 Jerusalem, Israel

\* See <http://west.cea.fr/WESTteam>

**Abstract:** The consequences of tungsten (W) melting on divertor lifetime and plasma operation are high priority issues for ITER. Sustained and controlled W-melting experiment has been achieved for the first time in WEST on a poloidal sharp leading edge of an actively cooled ITER-like plasma facing unit (PFU). A series of dedicated high power steady state plasma discharges were performed to reach the melting point of tungsten. The leading edge was exposed to a parallel heat flux of about 100 MW.m<sup>-2</sup> for up to 5 s providing a melt phase of about 2 s without noticeable impact of melting on plasma operation (radiated power and tungsten impurity content remained stable at constant input power) and no melt ejection were observed. The surface temperature of the MB was monitored by a high spatial resolution (0.1 mm/pixel) infrared camera viewing the melt zone from the top of the machine. The melting discharge was repeated three times resulting in about 6 s accumulated melting duration leading to material displacement from three similar pools. Cumulated on the overall sustained melting periods, this leads to excavation depth of about 230 μm followed by a re-solidified tungsten bump of 200 μm in the JxB direction.

**Keywords:** Tungsten melting, Plasma Facing Unit, Heat flux calculation, IR thermography

**Corresponding author address:** CEA, IRFM, F-13108 Saint-Paul-lez-Durance, France.

**Corresponding author e-mail:** yann.corre@cea.fr

### 1. Introduction

Due to the introduction of poloidal and toroidal gaps (0.5mm width) associated to the monoblock (MB) technology [1], magnetic field lines can penetrate into the gaps and intercept the poloidal leading edges (LEs) with near normal incidence [2]. In ITER, this leads to very high heat load especially during ELMs (several GW.m<sup>-2</sup>) but also during steady state or inter-ELM periods (hundreds of MW.m<sup>-2</sup>) [3]. Because of potential misalignment between plasma facing units [4] or in case of failure of the components in the machine, like armor-to-heat sink bounding defect affecting the heat removal capability of the component [5-6], the risk of transient or sustained melting becomes a major concern for ITER and next step fusion devices

Several experiments have been successfully carried out in both, limiter and divertor geometries, to investigate sustained (TEXTOR experiment using roof-like test-limiter [7]) or transient repetitive melting of tungsten (W) by ELM on special geometries, overexposed LEs as well as sloped lamella in AUG [8] and JET [9-10] tokamaks. These experiments have been performed with bulk tungsten but without active

cooling such as ITER-like PFU, therefore with a strong dependence on surface temperature and pulse history compared to actively cooled component once stationary surface temperature is established. Prolonged steady-state exposures resulting in large material displacement could offer an opportunity to enlarge the energy fraction expended on solid/liquid phase transition and to reduce the sensitivity of molten mass to input heat flux [11].

To achieve melting in WEST, a 2mm deep groove was machined in one of the actively cooled MBs and a series of dedicated high power steady state plasma discharges were performed to reach the melting point of tungsten ( $\approx 3420^\circ\text{C}$ ). The experimental set-up is presented in section 2. The sustained W-melting experiment ( $P^{\text{inj}} = 5.5 \text{ MW}$ ,  $I_p = 500 \text{ kA}$ ,  $B = 3.7 \text{ T}$ ) is presented in section 3. The experimental results including IR thermography analysis and post-mortem confocal microscopy to evaluate the melt displacement are presented in section 4.

## 2. Experimental set-up

One of the aims of the WEST tokamak is to test actively cooled ITER-like PFUs [12-13]. During the C5 experimental campaign, the WEST divertor was equipped with 76 PFUs on two different sectors, each composed of 35 tungsten ITER grade MBs. To achieve melting, a groove (30 mm long toroidally, 9 mm wide poloidally, and 2 mm deep) was machined in one of the MBs in order to expose the sharp LE of the adjacent downstream MB directly to the full incident parallel heat flux at the outer region of the target module (figure 1). The groove was machined on the maximum heat flux area regarding the toroidal ripple effect (PFU#7), in a remote location accessible with far outer strike point (OSP) magnetic configuration only (MB28, while usual OSP position lies between MB24 and 27). To gain in power load and get easier access to the melting point, the PFU chosen to melt (PFU#8) has been misaligned in the vertical direction ( $\delta = +0.3 \text{ mm}$ ) compared to the upstream one (PFU#7). The total length fully exposed to the parallel heat flux is therefore 2.3 mm (see figure 2.b). The far OSP equilibrium also enables to minimize the magnetic flux expansion and thus to maximize the heat flux intensity at the target.

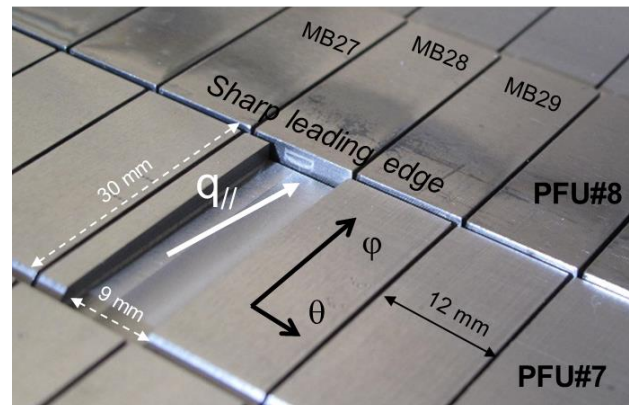


Figure 1: picture of the groove machined on PFU#7 to expose the sharp leading edge on the PFU#8.

The surface temperature of the MB was monitored by a very high spatial (VHR) resolution (0.1 mm/pixel) IR thermography system equipped with a medium-wavelength IR filter ( $3.9 \mu\text{m}$ ) viewing the melt zone from the top of the machine [14]. The VHR system has a field of view (FoV) covering  $\sim 2 \times 4$  MBs ( $64 \times 51 \text{ mm}$ ). The system is equipped with two orientable mirrors enabling to cover a wide surface of the divertor ( $\sim 13^\circ$  in the toroidal direction, corresponding to the area where ITER like PFU are installed, from PFU #6 to PFU #19) and the 2 strike point areas along the PFU in the poloidal direction (from MB #6 to #32). The IR system measured IR radiation and is calibrated using a black-body (BB) with surface emissivity  $\varepsilon=1$ . The spectral radiance of the surface MB ( $L^w$ ) is given by the following equation [15]:

$$L^w = L^{BB} \times \varepsilon_w + (1 - \varepsilon_w) \times L^{amb} \quad (1)$$

where  $L^{BB}$  is the spectral radiance of the BB (Planck radiation),  $\varepsilon_w$  is the surface emissivity of tungsten MBs and  $L^{amb}$  is the spectral radiance of the actively cooled ambient environment ( $T^{amb} = 70^\circ\text{C}$ ). True temperature are computed afterward using equation as function of temperature based on emissivity measurement [16]. The melting experiment and groove size have been designed to reach melting with

heat flux intensity obtained in WEST during the LE experiments performed in the previous experimental campaign (C4) [17]. Numerical modelling of the temperature was performed with a 3D finite element method (FEM) including ITER-like MB prototypes with 28 mm width (ITER standard width for thermal calculation) and 6 mm tungsten thickness [1] between the top surface and the CuCrZr cooling tube in steady state (figure 2).

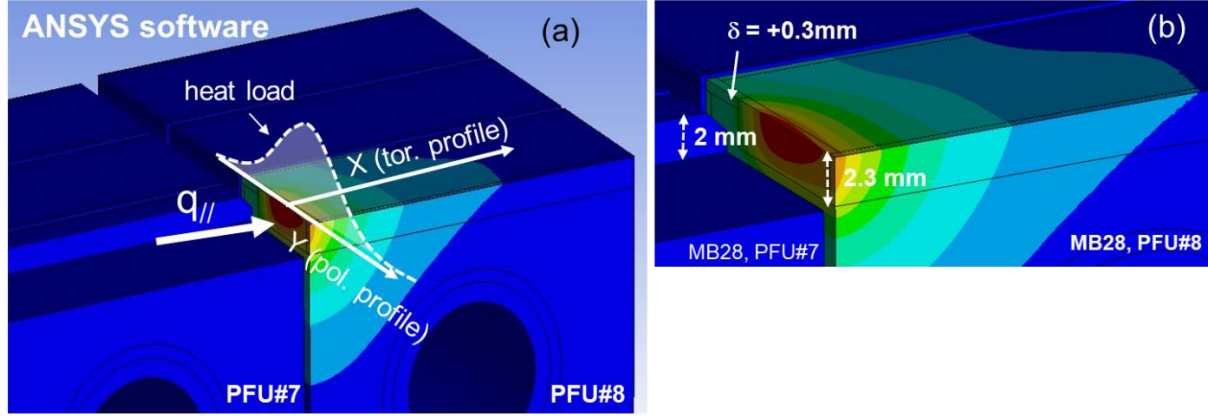


Figure 2: Thermal modelling assuming  $q_{//} = 107 \text{ MW}\cdot\text{m}^{-2}$ ,  $y_0 = 4.2 \text{ mm}$ ;  $\lambda_q = 10 \text{ mm}$ ,  $S = 1 \text{ mm}$  as depicted in equation (3). (a) full view showing the groove and the overexposed LE to be melt, (b) zoom on the overexposed sharp LE showing the vertical misalignment between PFU#7 and PFU#8.

The heat load is computed with the optical projection of the parallel heat flux on the MB surfaces:

$$q_n = q_{//} \cdot \sin \alpha \quad (2)$$

where  $\alpha$  is the angle between the magnetic field line and the MB surfaces. The heat flux distribution on the MB surfaces is computed using convolution of a Gaussian spreading with a truncated decaying exponential in the scrape off layer (SOL) as depicted in [18] and already validated in WEST [19]:

$$q_{//}(y) \propto \exp\left[\left(\frac{S}{2\lambda_q}\right)^2 - \frac{y-y_0}{\lambda_q}\right] \times \text{erfc}\left(\frac{S}{2\lambda_q} - \frac{y-y_0}{\lambda_q}\right) \quad (3)$$

Where  $y$  is the target position in the poloidal direction,  $y_0$  is the OSP location,  $\lambda_q$  is the local heat flux decay length on the target (i.e. not mapped to the outboard midplane),  $S$  is the heat flux spreading factor in the private flux region. The thermal modelling gives the spatial distribution of the surface temperature ( $T_{\text{FEM}}$ ) that is used afterward to compute the synthetic temperature ( $T_{\text{synth}}$ ) as seen by the IR camera as depicted in [20]. To simulate the pixel size, optical blurring and deformation, the numerical radiance profile (calculated from  $T_{\text{FEM}}$  using Planck equation) is convoluted with the transfer function of the instrument which is modelled by a Gaussian shape with a standard deviation  $\sigma = 0.175 \text{ mm}$  for the VHR system as mentioned in [21]. The parallel heat flux was adjusted to reach the melting point on the leading edge assuming heat flux decay length  $\lambda_q = 10 \text{ mm}$  on target (value obtain during C4 experiment with similar heating power) and position of the OSP  $y_0 = 4.2 \text{ mm}$  to get the maximum heat flux in the centre of the groove ( $y_{q\text{max}} = 6 \text{ mm}$ ). A very high temperature gradient is observed near the LE, almost  $700^\circ\text{C}$  temperature decrease over  $1 \text{ mm}$ . Because of the spatial filtering effect of the IR camera far small objects (smoothing of the sharp temperature variation), the real temperature ( $T_{\text{true}} = 3420^\circ\text{C}$  expected at the melting point) falls down to  $T_{\text{synth}} = 3076^\circ\text{C}$  as would have been measured by the instrument assuming BB emission, a decrease of  $\sim 345^\circ\text{C}$  compared to the true temperature (see figure 5-b). The maximum temperature measured on the synthetic profile is also located  $0.4 \text{ mm}$  away from the leading edge. The thermal modelling doesn't include the latent heat during melting as well as surface cooling effects due to vaporization and thermionic emission processes [22]. The calculation shows that we need at least  $107 \text{ MW}\cdot\text{m}^{-2}$  parallel heat flux projected on the target to reach melting.

### 3. WEST experiment

The aim of the experiment was to achieve high and stationary heat flux for at least  $5 \text{ s}$  to reach thermal equilibrium in the MB (the theoretical time constant to reach 95% of the stabilized temperature is  $2.4 \text{ s}$ )

and to get sustained melting for about two seconds. A far X-point magnetic equilibrium was developed to get the maximum heat flux location in the toroidally running groove located in MB28 keeping good RF coupling condition in front of the LHCD launchers. The magnetic strike point position is currently controlled with feedforward adjustment with accuracy of about 1 mm. As a consequence, increasing the input power, and so the Shafranov shift of the global magnetic equilibrium, led to an inward displacement of the peak heat flux toward MB 27. The X-point height was therefore adjusted pulse to pulse to keep the maximum heat flux in the center of the groove. The X-point height was moved from 102 mm at low power up to 112 mm during the melting experiment. The pulse scenario used during the melting experiment is displayed in figure 3. The plasma current is set to  $I_p = 500$  kA during more than 10s with magnetic field  $B_T = 3.7$  T. The heating power is injected from 5s up to 10s with the two LHCD launchers (a). Figure (b) displays the BB temperature as measured by the IR system during the melting experiment. 95% of the stabilized temperature is reached after about 2.5s which is consistent with numerical expectation. The melting phase lasts for about 2s, then the IR safety system was activated due to a hot spot on one of the two LHCD launchers and the melt was expected to re-solidify 0.6s second before the power cut-off. During melting phase, total radiated power ( $P^{rad} \sim 2.3$  MW) and tungsten impurity content evaluated with ultra-violet (UV) spectrometer ( $W^{43+}$  emission line) remained stable at constant input power (figure 3-a). No melt ejection was observed with the VHR IR system which is consistent with the sample post-exposure surface analysis results reported in figure (4).

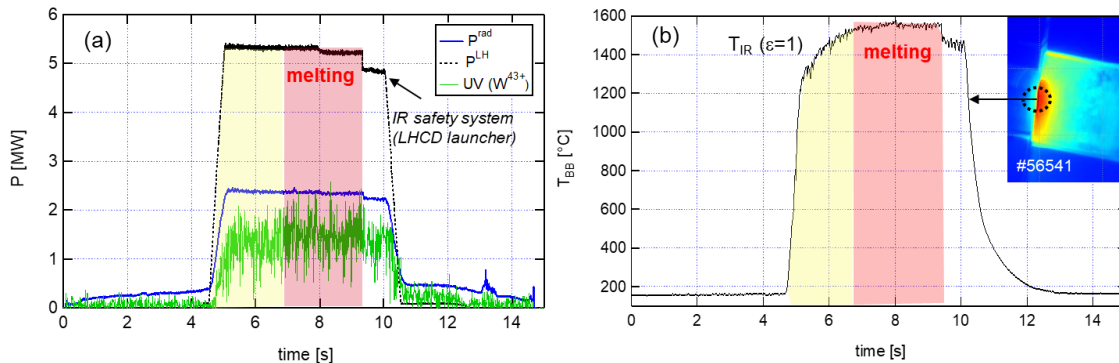


Figure 3: Injected power (Low Hybrid), radiated power measured with bolometry and UV emission measured in the core plasma at  $\lambda = 270.7$  Å, a line identified to be a second order from  $4s^24p^2P^{3/2} - 4s4p^2^2D^{5/2}$  transition for  $W^{43+}$  at 135.34 Å (a) and BB temperature (b) measured during the melting experiment (maximum value in the region of interest located in front of the groove in the centre of the MB) as function of time.

During the power increase, few pulses before reaching the melting point (with LE temperature clearly above the ductile-to-brittle temperature threshold), premature cracking has been detected with the VHR IR system thanks to local emissivity enhancement due to local cavity effect (figure 4 #56538). The melting was detected with the VHR IR thermography during the cooling phase: one can observe clear rounding of the LE, with a small hollow followed by a bump about 2 mm away from the melt point (figure 4 #56543), which is the consequence of material displacement as expected with the  $J \times B$  volumetric forces [22]. The pulse with melting conditions was repeated three times with similar injected energy to check the consequence of melting for plasma operation. The melt displacement results therefore in melting of three similar and consecutive pools (2s each, 6s of cumulated melt duration in total). In-situ visual inspection of the leading edge of the MB performed with the Articulated Inspection Arm (AIA) [23] confirm the melting of the LE in middle of the MB (figure 4).

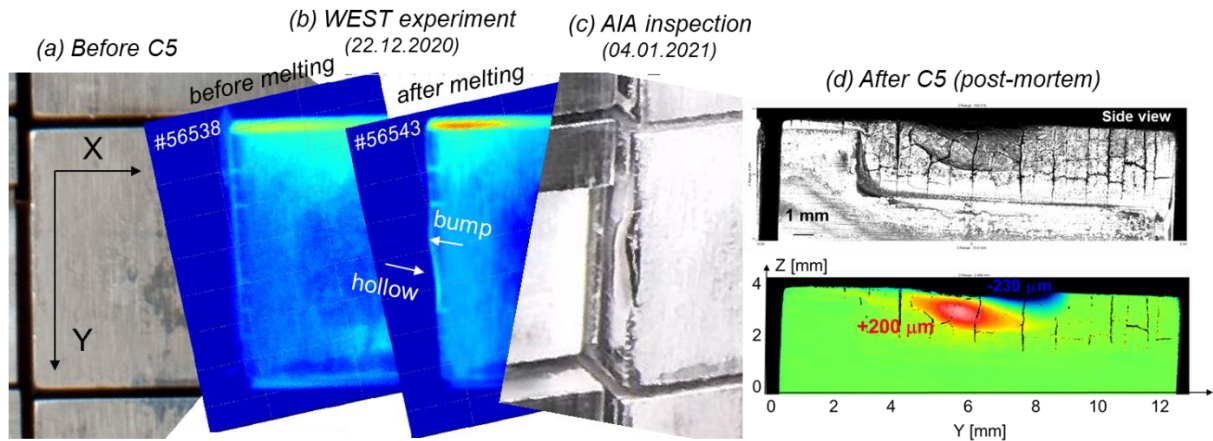


Figure 4: picture of the MB taken before the C5 experimental campaign (a), IR images taken during the cooling phase of the MB (b) few seconds after the power switch-off, before (#56538) and after melting (#56543), picture taken after the melting experiment with the AIA robot (c), and confocal microscopy (d).

#### 4. Experimental results

During the C5 experimental campaign, only two divertor sectors were equipped with actively cooled ITER-like PFUs (16% of the total surface covered). The other divertor sectors were equipped with W-coated graphite PFUs. The heat load was derived from standard IR thermography system looking at the W-coated graphite PFUs [19] and embedded thermocouples (TCs) [24]. During the W melting experiment, we found a parallel heat flux of about  $95 \text{ MW.m}^{-2}$  (IR data) and  $75 \text{ MW.m}^{-2}$  (TC data) and target heat flux decay length of 7 mm (IR data) and 10 mm (TC data) respectively, which represent slightly lower power load compared to the exposed LE. An image delivered by the VHR IR system during the melting phase (at 8s) is displayed in figure 5-a. The temperature profile extracted from the IR image along the toroidal direction is displayed in figure 5-b for comparison with FEM modelling. On the melting location, the BB temperature is found to be  $T_{\text{BB}}=1580^\circ\text{C}$  (black crosses) while synthetic data would predict  $3076^\circ\text{C}$  (blue crosses) due to the spatial filtering effect of the IR system assuming melting point is reached.

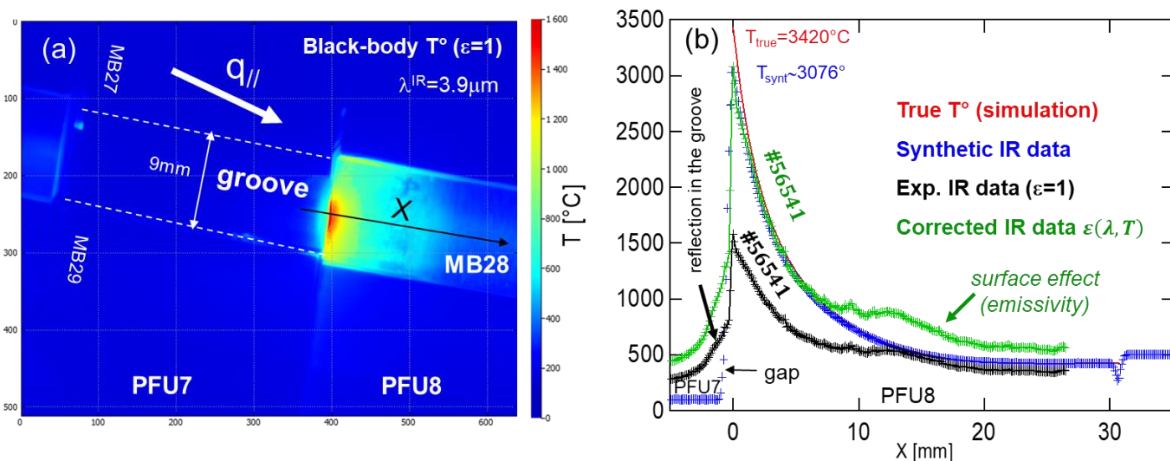


Figure 5: (a) VHR IR image during the melting experiment #56541 at  $t=8\text{s}$  when the thermal equilibrium is reached. (b) Temperature distribution along the toroidal direction: experimental IR data (black crosses), corrected (green crosses), synthetic (blue crosses) and FEM data (red line).

The guarantee to reach melting is used afterward as reference point to evaluate the emissivity of tungsten from equation (1). Here we found  $\epsilon = 0.32$  at  $\lambda_{\text{IR}} = 3.9 \mu\text{m}$  assuming  $T_{\text{true}} = 3420^\circ\text{C}$  and  $T_{\text{synt}} = 3076^\circ\text{C}$ . The emissivity is then extrapolated at lower temperature using laboratory emissivity measurements [15]. The full temperature profile is corrected using the extrapolated emissivity with

square root reduction scheme to derive the true temperature (green crosses). The experimental toroidal temperature profile is found to be consistent with synthetic data over almost 10 mm away from the LE, confirming the steep temperature gradient near the LE  $\sim 700^\circ\text{C}/\text{mm}$ . Significant discrepancy is found further away, in the middle of the MB, due to local surface effect generated by plasma wall interaction (erosion and deposition processes) and leading to potential increase of the emissivity [16]. The final surface deformation profile, measured with confocal microscopy after removal of the molten PFU from the machine, is presented in figure 4-d. A crater, 230  $\mu\text{m}$  deep and extending 2 mm along the poloidal direction, is found in the vicinity of the maximum heat flux location. The melt, moving from the location of initially induced pool, has re-solidified on the adjacent surface, forming a 200  $\mu\text{m}$  high bump. The displacement is consistent with flow in the JxB direction as predicted by MEMOS-U modelling [22]. The total melt displacement volume was evaluated to be 0.28  $\text{mm}^3$ . Such surface morphology explains the fact that no melt ejection was observed: the modest deformation and displacement signify that the melt pool was rather shallow and did not reach the PFU edge.

## 5. Conclusion

Sustained melting was achieved for the first time in WEST on ITER-like PFU under well controlled conditions. Radiated power and tungsten impurity content remained stable at constant input power, without noticeable impact of melting phases and no melt ejection was observed. The qualitative observation of the material displacement with the VHR IR camera, rounding the initially straight leading edge, was the first evidence of melting. In-situ visual inspection performed afterward with the AIA confirms the melting and its extension over two millimetres in the poloidal direction. VHR IR camera has been used to monitor the temperature distribution around the melted LE and compared to the thermal simulation. The melting point is used afterward to derive the emissivity of the tungsten which is used as a reference for extrapolation at lower temperature. Emissivity correction was performed to get true temperature along the MB. The modelled and experimental temperature gradients in the toroidal direction agree well with a value of about  $700^\circ\text{C}/\text{mm}$  near the melting zone. The heat load derived from the IR data analysis will be used as input to MEMOS-U code to model the melt dynamics at the actively cooled components under steady state plasma heat load. After removal of the melted component from the tokamak device, a melt displacement volume of 0.28  $\text{mm}^3$  has been determined by confocal microscopy. The observed bump of resolidified melt located next to the excavated melt crater is consistent with a flow in the JxB direction as predicted by MEMOS-U. Additional surface analysis, based on Scanning Electron Microscopy (SEM) and Electron BackScattering Diffraction (EBSD) measurements is ongoing to investigate the microstructure of the melted volume, the characteristic crack size and the tungsten grain size in both areas, crater and bump. The measurements collected during this experiment serve to further validate the underlying physics models of the MEMOS-U code in order to improve its predictive capability for the assessment of potential surface damage by accidental melt events in ITER in case of excessive heat loads.

## Acknowledgement

Work performed under EUROfusion WP PFC. This work has been carried out within the framework of the EUROfusion Consortium and has received funding from the Euratom research and training programme 2019-2020 under grant agreement No 633053. The views and opinions expressed herein do not necessarily reflect those of the European Commission.

## References:

- [1] T. Hirai et al. Design optimization of the ITER tungsten divertor vertical targets Fusion Engineering and Design. Volume 127, February 2018, Pages 66-72  
<https://doi.org/10.1016/j.fusengdes.2017.12.007>
- [2] J.P. Gunn et al. A study of planar toroidal-poloidal beveling of monoblocks on the ITER divertor outer vertical target. 2019 Nucl. Fusion 59 126043.  
<https://doi.org/10.1088/1741-4326/ab4071>
- [3] R. Pitts et al. Physics basis for the first ITER tungsten divertor.  
<https://doi.org/10.1016/j.nme.2019.100696>
- [4] R. Pitts et al. Physics conclusions in support of ITER W divertor monoblock shaping. Nuclear Materials and Energy. Volume 12, August 2017, Pages 60-74  
<https://doi.org/10.1016/j.nme.2017.03.005>
- [5] M. Missirlian, M. Richou, B. Riccardi, P. Gavila, T. Loarer, S. Constans. The heat removal capability of actively cooled plasma-facing components for the ITER divertor. Phys. Scr, 2011, Volume 145. 014080, 7 pp.

- 1  
2  
3  
4 [6] M. Ramaniraka: « Data cross-checking from ultrasound testing, IR thermography and high heat flux  
5 tests for the qualification of WEST PFU divertor ». This conference  
6 [7] G Sergienko et al. Experience with bulk tungsten test-limiters under high heat loads: melting and  
7 melt layer propagation. Phys. Scr. T128 (2007) 81–86  
8 [doi:10.1088/0031-8949/2007/T128/016](https://doi.org/10.1088/0031-8949/2007/T128/016)  
9 [8]. K. Krieger et al. Experiments on transient melting of tungsten by ELMs in ASDEX Upgrade. Nucl.  
10 Fusion 58 026024  
11 <https://doi.org/10.1088/1741-4326/aa9a05>  
12 [9] J. Coenen et al. ELM induced tungsten melting and its impact on tokamak operation  
13 Journal of Nuclear Materials, Volume 463, August 2015, Pages 78-8  
14 <https://doi.org/10.1016/j.jnucmat.2014.08.062>  
15 [10] J W Coenen et al Transient induced tungsten melting at the Joint European Torus (JET). Phys.  
16 Scr. 2017 014013  
17 <https://doi.org/10.1088/1402-4896/aa8789>  
18 [11] S. Ratynskaia et al. Resolidification-controlled melt dynamics under fast transient tokamak plasma  
19 loads. Nucl. Fusion 60 (2020) 104001 (7pp).  
20 <https://doi.org/10.1088/1741-4326/abadac>  
21 [12] J. Bucalossi et al., “The WEST project: Testing ITER divertor high heat flux component technology  
22 in a steady state tokamak environment,” *Fusion Engineering and Design*, vol. 89, no. 7, pp. 907–912,  
23 Oct. 2014, [doi:10.1016/j.fusengdes.2014.01.062](https://doi.org/10.1016/j.fusengdes.2014.01.062)  
24 [13] M. Missirliani, M. Firdaouss, M. Richou, P. Languille, S. Lecocq, and M. Lipa, “The WEST project:  
25 PFC shaping solutions investigated for the ITER-like W divertor,” *Fusion Engineering and Design*, vol.  
26 88, no. 9, pp. 1793–1797, Oct. 2013,  
27 [doi:10.1016/j.fusengdes.2013.03.048](https://doi.org/10.1016/j.fusengdes.2013.03.048)  
28 [14] M. Houry et al., “The very high spatial resolution infrared thermography on ITER-like tungsten  
29 monoblocks in WEST Tokamak,” *Fusion Engineering and Design*, vol. 146, pp. 1104–1107, Sep. 2019,  
30 [doi:10.1016/j.fusengdes.2019.02.017](https://doi.org/10.1016/j.fusengdes.2019.02.017)  
31 [15] J. Gaspar et al., “In-situ assessment of the emissivity of tungsten plasma facing components of  
32 the WEST tokamak,” *Nuclear Materials and Energy*, vol. 25, p. 100851, Dec. 2020,  
33 [doi: 10.1016/j.nme.2020.100851](https://doi.org/10.1016/j.nme.2020.100851)  
34 [16] J. Gaspar et al., “ Emissivity measurement of tungsten plasma facing components of the WEST  
35 tokamak” *Fusion Engineering and Design*, vol. 149, p. 111328, Dec. 2019.  
36 [doi: 10.1016/j.fusengdes.2019.111328](https://doi.org/10.1016/j.fusengdes.2019.111328)  
37 [17] A. Grosjean et al. Very high-resolution infrared imagery of misaligned tungsten monoblock edge  
38 heating in the WEST tokamak. *Nuclear Materials and Energy* 27 (2021) 100910  
39 [doi: 10.1016/j.nme.2021.100910](https://doi.org/10.1016/j.nme.2021.100910)  
40 [18] T. Eich et al. Empirical scaling of inter-ELM power widths in ASDEX Upgrade and JET. *Journal of*  
41 *Nuclear Materials*. Volume 438, Supplement, July 2013, Pages S72-S77.  
42 <https://doi.org/10.1016/j.jnucmat.2013.01.011>  
43 [19] N. Fedorczak et al. Cross diagnostics measurements of heat load profiles on the lower tungsten  
44 divertor of WEST in L-mode experiments. *Nuclear Materials and Energy*. Volume 27, June 2021,  
45 100961  
46 <https://doi.org/10.1016/j.nme.2021.100961>  
47 [20] Y. Corre et al., “Methodology for heat flux investigation on leading edges using infrared  
48 thermography,” *Nucl. Fusion*, vol. 57, no. 1, Art. no. 1, Oct. 2016,  
49 [doi:10.1088/0029-5515/57/1/016009](https://doi.org/10.1088/0029-5515/57/1/016009)  
50 [21] A. Grosjean et al. Interpretation of temperature distribution observed on W-ITER-like PFUs in  
51 WEST monitored with a very-high-resolution IR system. *Fusion Engineering and Design* 168 (2021)  
52 112387 [doi: 10.1016/j.fusengdes.2021.112387](https://doi.org/10.1016/j.fusengdes.2021.112387)  
53 [22] E Thorén, S Ratynskaia, P Toliás, R A Pitts. The MEMOS-U code description of macroscopic melt  
54 dynamics in fusion devices  
55 *Plasma Phys. Control. Fusion* 63 03502  
56 <https://doi.org/10.1088/1361-6587/abd838>  
57 [23] V. Bruno et al. WEST regular in-vessel Inspections with the Articulated Inspection Arm robot.  
58 *Fusion Engineering and Design*. Volume 146, Part A, September 2019, Pages 115-119.  
59 <https://doi.org/10.1016/j.fusengdes.2018.11.050>  
60 [24] J. Gaspar et al. First heat flux estimation in the lower divertor of WEST with embedded thermal  
61 measurements. *Fusion Engineering and Design*. Volume 146, Part A, September 2019, Pages 757-  
760 <https://doi.org/10.1016/j.fusengdes.2019.01.074>